A new method to achieve tens of nm axial super-localization based on conical diffraction PSF shaping

Clément Fallet[a], Maxime Dubois[a], Stephane Oddos[a], Roger Persson[a], Julien Caron[a], Jean-Yves Tinevez[b], Spencer L. Shorte[b], Gabriel Y. Sirat[a]

[a]Bioaxial SAS, 24 rue du Faubourg St Jacques, Paris, FRANCE;
[b]Institut Pasteur, 25 rue du Dr Roux, Paris, FRANCE;

ABSTRACT

We present here a new method based on conical diffraction for Z-super-localization. Using conical diffraction in a thin crystal we could shape the PSF so that it exhibits significant variations along the z-axis, and through an estimator we measure the position of the emitter. We study how this PSF could be used for single molecule imaging with a global assessment of the PSF by Fisher information analysis.. Preliminary experiments demonstrated that we could obtain the axial position with accuracy up to one tenth of the Rayleigh range. This technique would lead to resolutions of tens of nm with the use of high NA microscope objectives. Moreover it is fully compatible with 2D super-resolution imaging systems, which it could easily be coupled to.

Keywords: PSF shaping, CRLB, conical diffraction, single molecule imaging

1. INTRODUCTION

With the spectacular momentum of popularity known by fluorescence microscopy in biological research, several methods to improve the resolution of microscopes have been developed. Thus, the resolution limit of around 300nm coming from diffraction could be bypassed by methods such as fluorescence photo-activated localization microcopy (PALM)[1] and stochastic optical reconstruction microscopy (STORM).[2] These technique based on wide-field imaging of sparse single-molecule emitters can provide 2D resolutions under 50 nm. Unfortunately, with the features of standard PSF the resolution in axial dimension could not be improved as much as laterally. To overcome this effect, methods based on PSF shaping were developed to provide 3D Super Resolution information. For instance, with a mask in Fourier Plane, a double helix PSF can yield the lateral and the axial position of an emitter.[3,4] Recent developments of this technique highly improved axial positioning accuracy.[5] Similarly, an astigmatic lens can create PSFs that varies along Z, and the position of the emitter can be measure using this feature.[6] To compare these methods, a calculation of the Cramer-Rao lower bound (CRLB) is usually implemented.[7] Using this tool, the methods can be compared with criteria based on range or resolution. In this paper we show that PSF shaping can also be done by conical diffraction as already done in the excitation path in.[8–10] Similarly Z varying patterns can be obtained and implemented in the detection path of the microscope. After preliminary experiment we used CRLB calculations to tune the parameters used in the method. A discussion on the advantages and drawbacks of this technique concludes the paper.

2. PSF SHAPING WITH CONICAL DIFFRACTION

Conical diffraction occurs when light is sent on a biaxial crystal along one optical axis. However, if a quick analysis from Maxwell equation allows understanding when conical diffraction occurs, it is not sufficient to characterize entirely the phenomenon. Therefore we are using the theory developed by Berry (which originates from Maxwell theory though), leading to equations found in Berry's seminal paper,[11] so that we possess all the tools to carry out simulations on conical diffraction.

Observing again the equation (1) from our previously published proceeding,[10] we can see that the Electric Field is given by :

Further author information: (Send correspondence to Clement Fallet)
Clement Fallet: E-mail: clement.fallet@bioaxial.com, Telephone: +33 6 7827 2922

$$\mathbf{E}(\mathbf{R}, Z) = \left[B_0(R, R_0, Z) Id + B_1(R, R_0, Z) \begin{pmatrix} \cos\theta & \sin\theta \\ \sin\theta & -\cos\theta \end{pmatrix} \right] \begin{pmatrix} e_x \\ e_y \end{pmatrix}, \tag{1}$$

where B_0 and B_1 are beams associated with Bessel functions of zero and first order respectively:

$$B_0(R, R_0, Z) = k \int_0^\infty \mathrm{d}PPa(P) e^{-\frac{\mathrm{i}kZP^2}{2}} \cos(kR_0P) J_0(kRP),$$

$$B_1(R, R_0, Z) = k \int_0^\infty \mathrm{d}PPa(P) e^{-\frac{\mathrm{i}kZP^2}{2}} \sin(kR_0P) J_1(kRP),$$

From this equation, we can implement a simulation tool using MATLAB©.

2.1 Shaping the PSF

By using circular polarizers at crystal input and output, we could separate the two beams going out of the crystal. If we remove the second circular polarizer after the crystal, then the beam is composed of two components B_0 and B_1 that are added together and create a pattern which is the simple sum of the two patterns. This sum is in fact an incoherent sum where it is the intensities of the two patterns which are added. The sum is incoherent because we recall that the two exiting beam have an othogonal polarization so that they do not interfere. This fact becomes false when a linear polarizer is placed at the output of the crystal. With such a device, the two beams are projected on the same polarization basis and therefore they interfere. To understand how these two beams interfere, we need to observe the respective phase of the two beams. Figure 1 with arrows showing both phase and intensity of the beams are useful to understand how the two beams interfere. On the resultant pattern, we can see that the singularity of phase in the middle of the Vortex beam is shifted by the uniform phase of the Fundamental beam. As a result, the intensity is not invariant by rotation anymore.

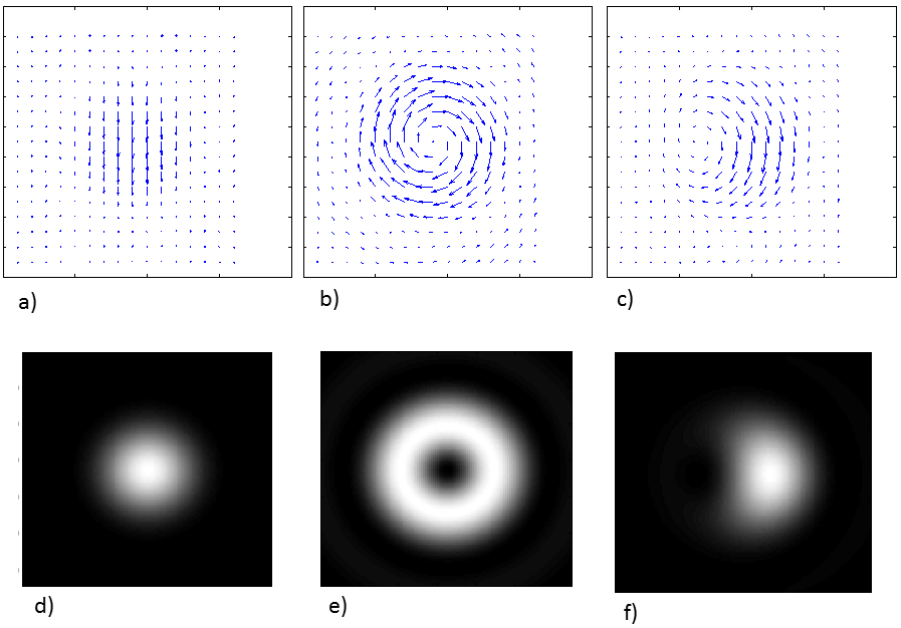

Figure 1. Representation of a fundamental beam a) and d) , a vortex beam b) and e), and the addition of the two beams c) and f).

Elliptical polarizers. We can see these beams as the sum of four different beams which are two Fundamental beams and two Vortex beams. The two Vortex beams have an opposite phase handedness (one comes from a left circularly polarized beam and is transformed by the crystal into a right circularly polarized light the same thing happens in the opposite way for the second beam, leading to opposite handedness of Vortex) ; and the two Fundamental beams have a constant phase. We can see that rotating a linear polarizer has a rotational effect on the phase map of the beams. Thus we understand that for one value $\Delta\theta_+ = 0°$ of the two Fundamental beams are in phase, and for another value $\Delta\theta_- = 90°$ the two fundamental beams are in opposition of phase and cancel. As a result at $\Delta\theta = \Delta\theta_-$, the resulting beam is the sum of only two Vortex beams with opposite phase handedness. The resulting intensity profile is composed of two intense lobs with a zero intensity between them that we call half-moons.

In fact, instead of limiting ourselves to linear and circular polarizers, we more generally use elliptical polarizers which are the simple addition of a linear polarizer and a Quarter Wave Plate. The pattern generated, can be seen as previously as the coherent sum of four beams (two Vortex beams and two Fundamental beams) with varying orientation and intensity. In fact, an elliptical polarization state can be seen as the sum of two opposite circular polarization state of different intensity so that the same four beams described before play a role in the final pattern with different contribution. The case of the Half-Moons pattern is a particular case obtained for four beams of same intensities and special orientation leading to the cancelation of the two fundamental beams. By playing with all this parameters we could generate a great number of different patterns. We show some of them in figure 2 where all the patterns are obtained for orientation of the elliptic polarizers at $\Delta\theta = 90°$.

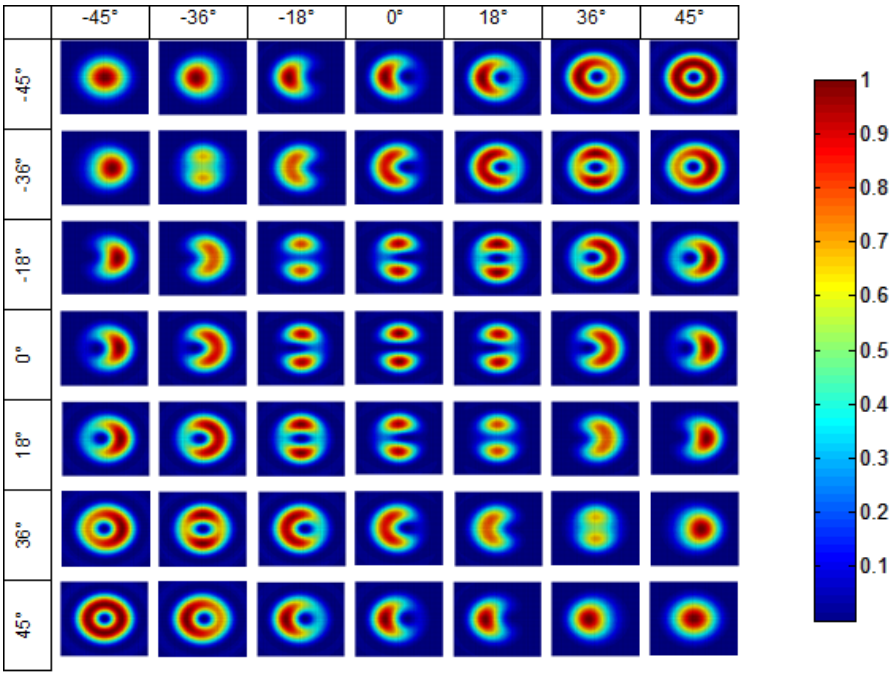

Figure 2. Table showing several patterns in the focal plane, obtained with elliptic polarizer with orthogonal orientations of their fast axis and varying ellipticity.

2.2 Z-varying PSF

We demonstrated how conical diffraction could shape the classical Airy PSF into various patterns. Quick observations were made to observe their variations in z at the scale of a standard Airy PSF. Some patterns showed no variation, the shape of the pattern staying the same while the intensity decreases with defocus (e.g. Vortex distributions or Half-Moons). Other patterns showed variations of shape with defocus that draw our attention. In the following we describe and provide an analysis of those Z-varying PSFs.

Stokes PSF. The PSF obtained from a linear polarizer at crystal input and circular polarizer at crystal output is one of those PSFs. We named it Stokes PSF, and we observed the pattern in focal plane on figure **??**. We recall that it is the coherent addition of a Vortex beam and a Fundamental beam. We saw previously that the effect of the fundamental beam on the Vortex beam was to shift the phase singularity. This effect goes on after and before the focal plane but with defocus the phase of the Fundamental beam varies less rapidly than the one of the Vortex beam, so that the place of destructive interference also rotates. Figure 3 illustrates this effect.

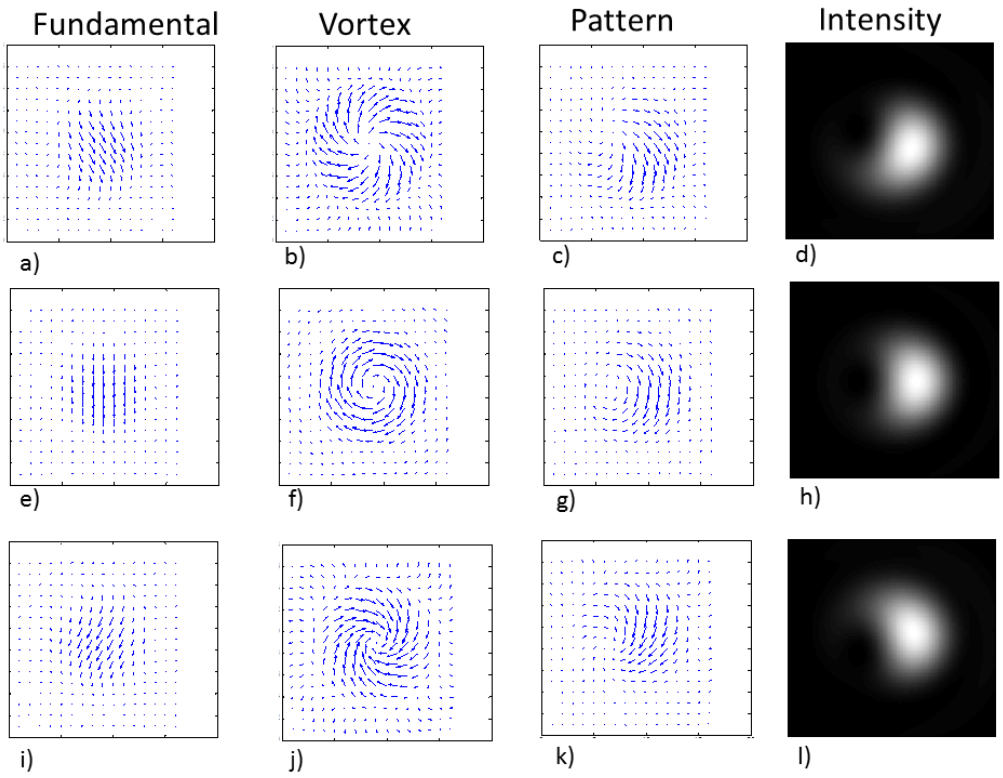

Figure 3. Simulation of patterns obtain at ρ_0=0.45 before focal plane (Z=-0.2Z_{Airy} a) to d)), at focal plane (Z=0; e) to h)) and after focal plane (Z=0.2Z_{Airy} i) to l)). The Stokes pattern (c,d,g,h,k,l) is the addition of a Vortex beam (b f and j) and an Fundamental beam (a e and i).

Shifted-Moons pattern. A second pattern that draws our attention is a pattern obtained with two elliptic polarizers oriented at 90°and same ellipticity. The global pattern is in fact the coherent addition of the usual Half-Moons pattern with two fundamental beams out of phase that do not cancel because of their different intensity. Once again, we can see that the phase of the fundamental changes less quickly with defocus than the phase of the Half-Moons. Figure 4 highlights this effect. As a result the constructive interference between the fundamental beam and the Half-Moons beam varies with defocus. In the following, we refer to this pattern as the Shifted-Moons patterns.

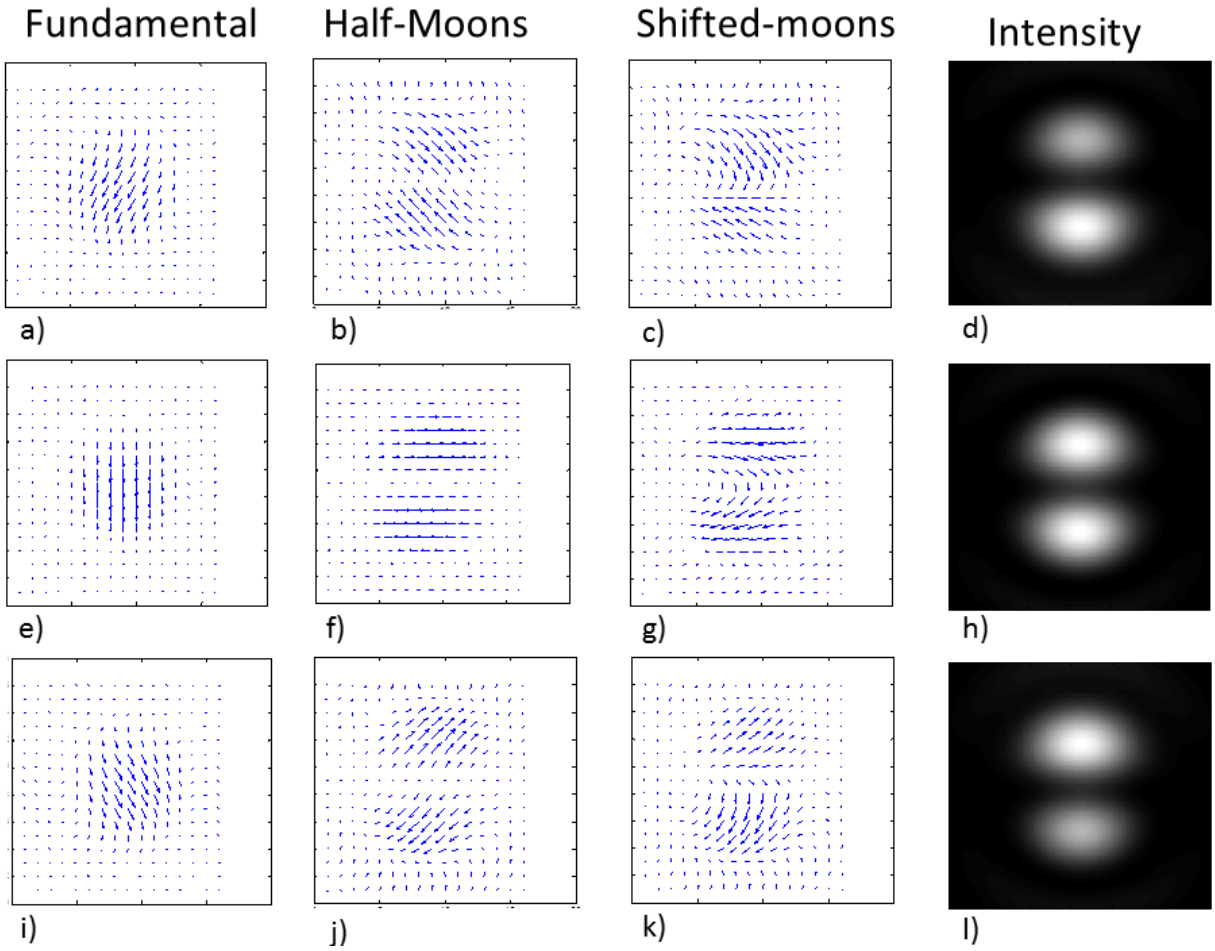

Figure 4. Simulation of patterns obtain at ρ_0=0.45 before focal plane (Z=-0.2Z_{Airy} a) to d)), at focal plane (Z=0; e) to h)) and after focal plane (Z=0.2Z_{Airy} i) to l)). The Shifted-Moons pattern (c,d,g,h,k,l) is the addition of a Half-Moon pattern (b f and j) and an Fundamental beam (a e and i).

2.3 Experimental validation

We could set up an optical bench to observe these patterns. Instead of using a fluorescent single emitter like a fluorophore or a quantum dot, we used a Point Source as an emitter. The Point Source is generated by focusing a collimated laser beam with a high quality microscope objective (Leitz 50X/0.85 P) mounted on a translation stage so the axial position of the Point Source can be adjusted. A $1:1$ telecentric relay system focuses the light in a 0.8mm thick slab of LBO crystal. The same relay system images the Focal Image Plane on the camera. The advantage of a dual telecentric relay system is the ability to insert very easily any polarizing element so the state of polarization of the incoming/outcoming light can be controlled very accurately and uniformly. Figure 5 shows a scheme of the set-up and the intensity distributions we could generate and observe thanks to it. These distributions showed the same Z-variations as the simulated one.

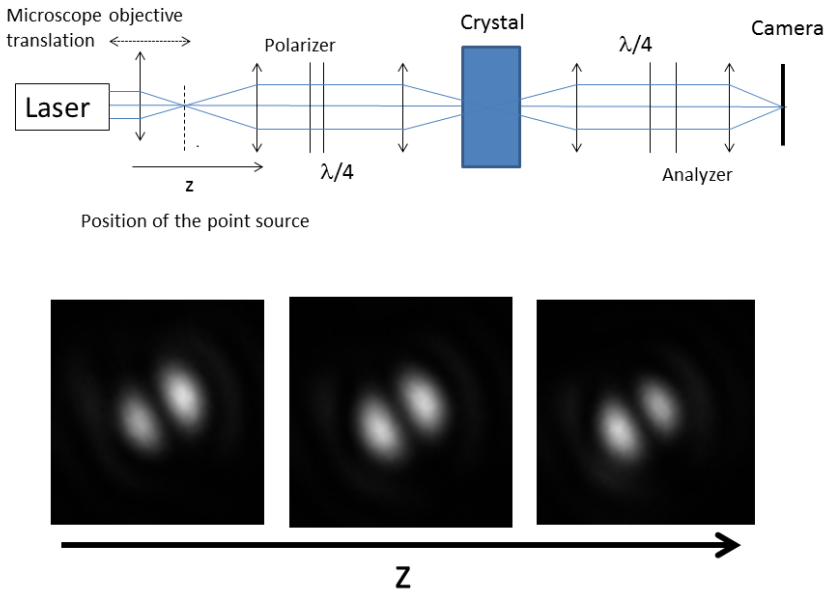

Figure 5. Top: Scheme of the set-up to observe Z-varying distributions. Bottom: images on the camera of the generated distributions for different values of z

3. SINGLE MOLECULE IMAGING WITH CONICAL DIFFRACTION

3.1 Choice of an estimator

This Z-varying patterns recall the techniques used in PALM and STORM to obtain information on the axial position of fluorophores. The same principle could be applied with the Z-varying pattern obtained by using conical diffraction. The axial position of a fluorophore could be measured by observing the pattern obtained in a lateral slice with a camera, as shown by figure 6. To know the position of the emitter, a estimator has to be chosen. Among several possibilities we chose an estimator that cumulated the advantages of being noise-tolerant, anti-symmetric in respect to the focal plane, and nearly linear near the focal plane. In the case where the Shifted-Moons pattern is used, a simple intensity ratio of the two lobs can give the axial position of the emitter. The idea could be apply to the Stokes pattern, where a measure of the orientation of the dark point could give the axial position of the emitter. In the following of this section, we will analyze the theoretical localization accuracy an estimator based on these distributions could reach. To do so, following the methodology of the literature, we will compute the Cramer-Rao lower bound of the Fisher information.

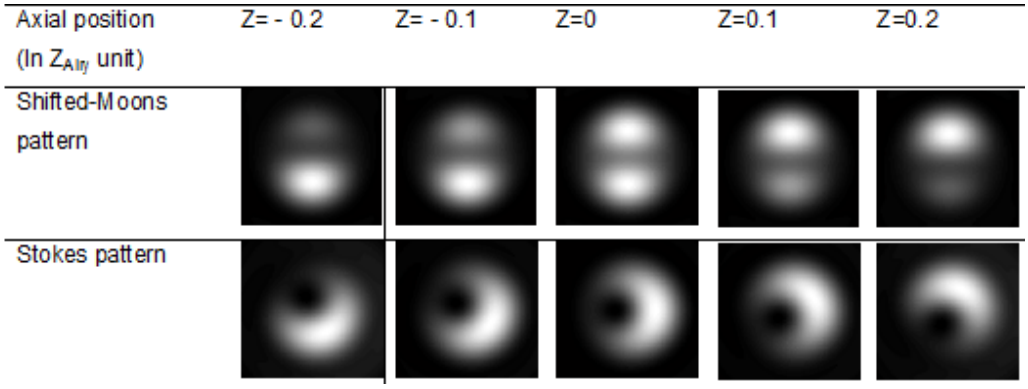

Figure 6. Simulated patterns for different defocus of emitter.

To compute this estimator from an image, the following steps are done:

- Identify two local maxima corresponding to the maximum of each lob
- Crop the image to a disc centered in the middle of the two maxima, with a diameter of 3 times the distance between the two maxima.
- Create a logical mask that equals one for the 1% of higher intensity pixels of each area and zero for other
- Identify the two part of the mask, which leads to two masks each corresponding to one lob.
- Multiply each of these masks with the initial image which leads to two images with only one lob in each.
- For each resulting image, sum the values of each pixel which leads to two scalar I_1 and I_2
- Compute the value $R = 100 \times \frac{I_1 - I_2}{I_1 + I_2}$

We first applied this steps to the simulation images. We obtained the curve presented in figure 7 which as mentioned before has a linear behavior near the focal plane (bending point in Z=0) and is anti-symmetric. We consider that this estimator is noise-tolerant because it is calculated from an area of pixels (and not only one pixel), and these pixels are those receiving a signal much higher than the background noise.

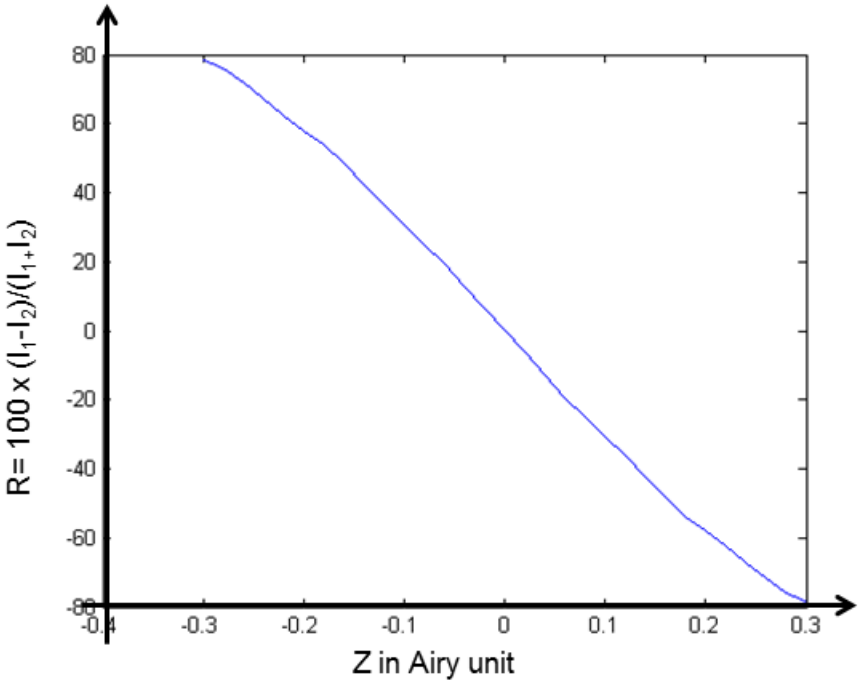

Figure 7. Ratio of the lobs of the simulated Shifted-Moons pattern.

From the process described previously, we tried to quantify what would be the effect of noise on the estimator. However, when considering the steps implied in the process we could not find an analytical relation between the estimator and the SNR. From this statement, stayed one way to quantify the effect of noise on the value of the estimator, which is the stochastic way. If we did not add to our simulated images a varying noise to observe its effect on the estimator, we did an experimental study with our set-up, and for several positions of emitter we took thousands of images to see the variation of the estimator with the noise. With this step, we could determine the statistic error of the estimator and relate it to an standard error in the position of the emitter. The final curve obtained with the previously described estimator applied on the experimental images, with errors bars

corresponding to experimental standard errors, is shown in figure 8. The conclusion of this experiment is that with this lay out we were able to measure the position of a an emitter from one image, with an accuracy of 20 microns corresponding to $0.006Z_{Airy}$. However, such accuracy with real fluorophores would be difficult to obtain because the fluorescent light would be weaker than the light coming from our experimental point light originating from a laser. Consequently, the Signal Noise Ratio would be less good leading to a worse accuracy in the calculation of the ratio of intensity between the two lobs of the pattern, and in the end a worse accuracy on the estimated axial position.

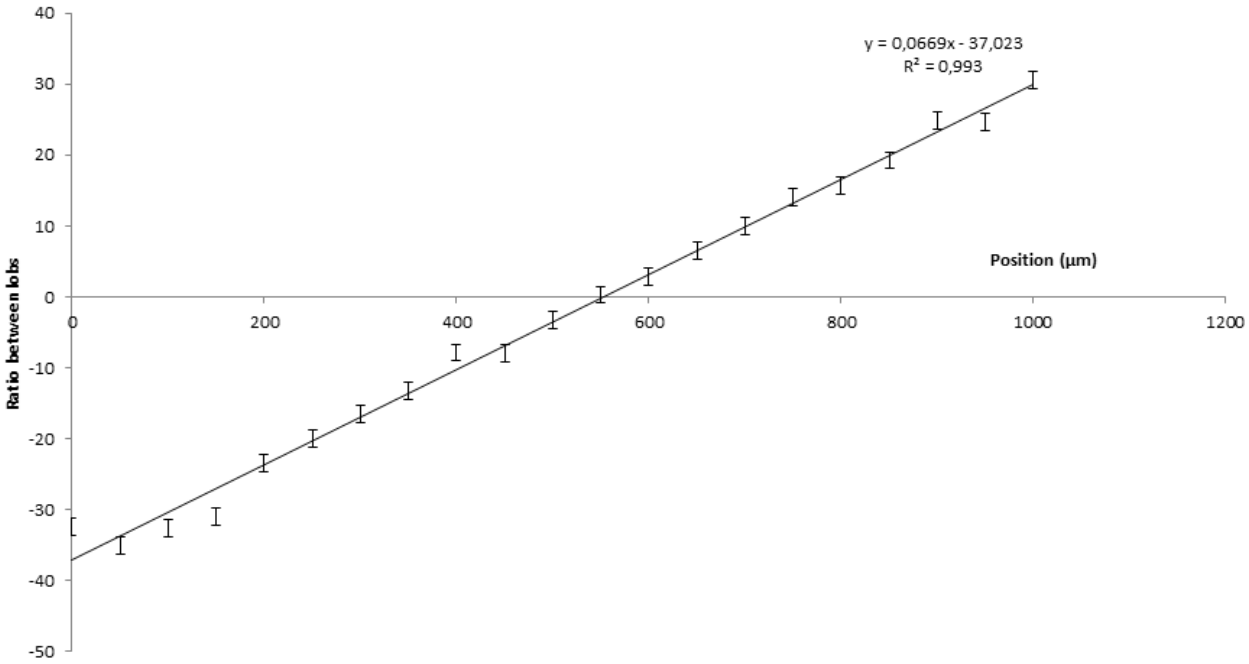

Figure 8. Estimator calculated from the experimental patterns.

3.2 CRLB calculation

To be able to assess how effective would be the use of this PSF in a 3D super-localization scheme, we introduce the tools commonly used to quantify relevant parameters of the PSF. From statistical information theory, the effectiveness of a PSF for encoding the position of an emitter is based on Fisher information,[12] a mathematical measure of the sensitivity of a quantity (the intensity) to changes of a parameter (defocus). With the Fisher information function, we can compute the Cramer-Rao lower bound (CRLB), which is the theoretical best precision that can be achieved with an unbiased estimator. This best precision may be obtained in practice with a good estimator, but this is independent of the CRLB calculation.

Many articles recently reported the performances of 3D super-localization scheme for different PSF-shaping methods including Double-Helix, Biplane and Astigmatism.[5,7,12] We implemented this calculation for two different PSF types: for an PSF showing astigmatism to have a reference measure to compare our method to and a PSF shaped with conical diffraction. To to so we first compute the 3D PSF resulting of a pupil sampled to a 256×256 grid, with steps of defocus of 250nm.

For the standard PSF calculation, the pupil in Fourier-plane is given by $P(x'y') = circ(r/R)$ for an emitter on axis,where R is the radius of the pupil plane, $circ(\eta) = \left\{ \begin{array}{l} 1, \eta < 1 \\ 0, \eta \geq 1 \end{array} \right\}$

.

For the PSF showing astigmatism we start from a pupil $P(x'y') = circ(r/R) \times exp(iAST(r))$ where AST(r) accounts for the introduction of astigmatism, with $AST(r) = c_{AST}\sqrt{6} \times r^2.cos(2\theta)$ with c_{AST} a coefficient to quantify astigmatism

For the PSF obtained by conical diffraction :

$$P(x'y') = circ(r/R) \times \left[cos(kR_0P) - isin(kR_0P) \times \begin{pmatrix} \cos\theta_p & \sin\theta_p \\ \sin\theta_p & -\cos\theta_p \end{pmatrix} \right] a(P) \tag{2}$$

The image formation model, using u, v for the real space coordinated at the detector plane, is derived from the Fresnel approximation and the intensity at the detector plane I_p is given by :

$$I_p(u,v) \propto \left| FT \left\{ P(x',y').exp(\frac{-i\pi\alpha M^2 z r^2}{\lambda f^2}) exp(\frac{2i\pi M(xx'+yy')}{\lambda f}) \right\} \right|^2 \tag{3}$$

In this expression, the first exponential term accounts for the quadratic phase induced in the pupil plane when an emitter is at a distance z from the focal plane. The second exponential term is a linear phase-ramp used to account for the lateral displacement of the emitter whose position is encoded by parameters (x,y,z). f is the tube lens focal length, $\lambda = 560nm$ is the peak emission wavelength and M=100 is the magnification. The parameter $\alpha = 0.81$ is used to augment the Fresnel propagation model to account for defocus in a high-index immersion medium (n=1.518), and better approximate the phase of the light propagating through a non-paraxial optical system. We used a pupil plane radius of R=2.15 mm. Remark that the coordinate scaling is such that camera coordinate (u, v) correspond to the Fourier plane frequencies $(u/\lambda f, v/\lambda f)$. Additionally, the actual measured image is pixelated, due to the finite pixel size of the detector. For a given pixel size of $16\mu m$, the PSF appearing on the camera is finally obtained with an interpolation to the right scale. The number of camera pixel is chosen to be Np=64. Finally a normalization step is operated in order to have a total number of photon N_{ph} per frame, when summing over all the pixel of one plane z.

We finally obtain the value $\mu(z,k)$ of the detected PSF model for each pixel (k). To compute the Fisher information, we assume an additive Poisson noise and a constant background of β, for a point source along the optical axis is given by :

$$I_{Fisher}(z) = \sum_{k=1}^{Np} \frac{1}{\mu(z,k) + \beta} \left(\frac{\partial \mu(z,k)}{\partial \theta} \right)^T \left(\frac{\partial \mu(z,k)}{\partial \theta} \right) \tag{4}$$

where $\theta = (x, y, z)$ is the position of the emitter.

3.2.1 Astigmatic PSFs

We ran the calculation for a astigmatic PSF, in order to compare the two similar methods. In this case there is no photon loss, and the accuracy obtained by this method is very good. These results are consistent with previously published results by different groups.[5,7] Figure 9 here is given for the sake of comparison only. The set of parameters chosen for the simulations is the same as in one of the latest reference on the subject.[5]

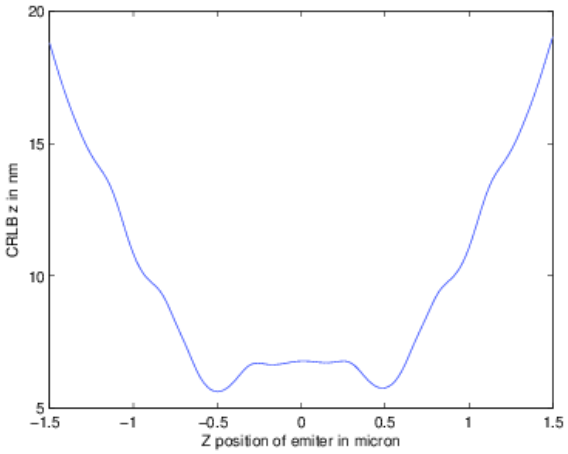

Figure 9. $CRLB_z$ of a PSF shaped by astigmatism with parameter c_{AST}=20000

3.2.2 Optimization of PSF obtained by conical diffraction

We ran the calculation for the shifted-moons PSF with different parameters for the PSF generated by conical diffraction. The parameters implied are the crystal thickness and the polarization states generator and analyzer at crystal input and output. Several optimizations were made, depending on the range targeted, but in all case, we tried to obtain the lowest more uniform CRLB over a fixed range. Two ranges were studied : 3 microns, and 1 micron. In each case we found the best value of parameter (crystal thickness, ellipticity of polarizers). Figure 10 and 11 show the CRLB curves obtained.

It is striking to observe that the general values for the CRLB are higher than the general values obtained for a astigmatic PSF. This is due to the loss of photons implied by PSF shaping by conical diffraction. Indeed, as the fluorescent light is widely regarded as not polarized at first (an assertion that could be questioned), one half of the photons are lost after the first polarizer and then another quantity of the remaining photons is lost after the analyzer. This quantity varies with the parameters (ellipticity and crystal thickness) implied in the PSF shaping. Though the first photon loss due to the polarizer can be reduced thanks to clever polarization engineering, we added in the algorithm a mechanism to take into account the loss of photons in the shaping process, so that in the end a reduced number of the photon reached the camera. This number vary with the parameters, but is generally around 30% of the initial amount of photon (3500 photons in our calculations). This explain why the value of the CRLB is higher for the PSF shaped by conical diffraction. Still, the shaping allow to reduce the peak of the CRLB so that the value obtained with conical diffraction are far below the pic value of the CRLB obtained with a standard PSF.

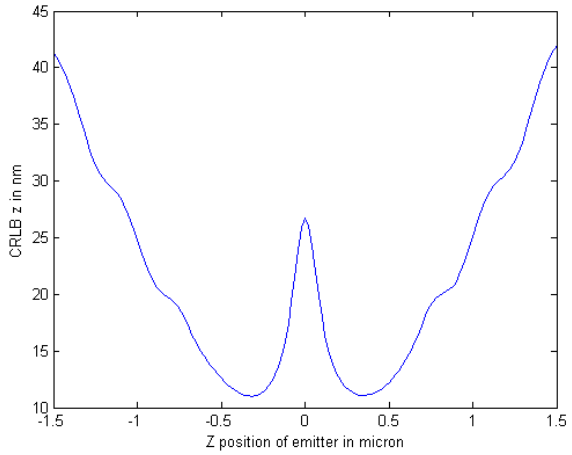

Figure 10. $CRLB_z$ of a PSF shaped by conical diffraction with an ellipticity parameter of 10 degree and crystal thickness parameter of 1mm. This PSF is good for operating at a range of $3\mu m$

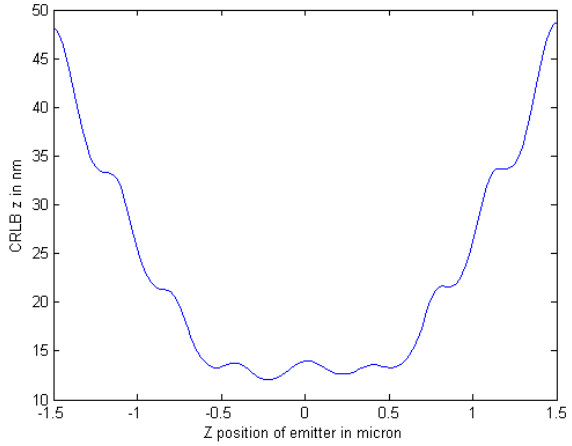

Figure 11. $CRLB_z$ of a PSF shaped by conical diffraction with an ellipticity parameter of 20 degree and crystal thickness parameter of 0.8mm. This PSF is good for operating at a range of $1\mu m$

4. DISCUSSIONS AND CONCLUSION

- meaning of CRLB = local variation, may be unadapted to represent the global variation of a PSF (in particular for Airy pattern)
- The rejection of photon because of the polarizers in the shaping by conical diffraction clearly limit its action
- However the change of shape of the CRLB curve can be made nearly uniform on a short range
- Beside, conical diffraction is simple to implement (compared to SML)
- Moreover CRLB means best precision, but seems very far from practical result
- Is it possible to consider that one emiter emits non-uniform polarised light?

REFERENCES

[1] Betzig, E., Patterson, G. H., Sougrat, R., Lindwasser, O. W., Olenych, S., Bonifacino, J. S., Davidson, M. W., Lippincott-Schwartz, J., and Hess, H. F., "Imaging Intracellular Fluorescent Proteins at Nanometer Resolution," *Science* **313**, 1642–1645 (Sept. 2006).

[2] Rust, M. J., Bates, M., and Zhuang, X., "Sub-diffraction-limit imaging by stochastic optical reconstruction microscopy (STORM)," *Nat Meth* **3**, 793–796 (Oct. 2006).

[3] Pavani, S., "Three-dimensional, single-molecule fluorescence imaging beyond the diffraction limit by using a double-helix point spread function," *PNAS* **106**(9) (2009).

[4] Grover, G. and Quirin, S., "Photon efficient double-helix PSF microscopy with application to 3D photo-activation localization imaging," *Biomedical Optics Express* **2**(11), 3010–3020 (2011).

[5] Shechtman, Y., Sahl, S. J., Backer, A. S., and Moerner, W. E., "Optimal Point Spread Function Design for 3D Imaging," *Phys. Rev. Lett.* **113**, 133902 (Sept. 2014).

[6] Huang, B., Wang, W., Bates, M., and Zhuang, X., "Three-dimensional super-resolution imaging by stochastic optical reconstruction microscopy," *Science* **810**(2008) (2008).

[7] Grover, G., Pavani, S., and Piestun, R., "Performance limits on three-dimensional particle localization in photon-limited microscopy," *Optics letters* **35**(19), 3306–3308 (2010).

[8] Sirat, G., "FR2966258A1," (2010).

[9] Caron, J., Fallet, C., Tinevez, J.-Y., Moisan, L., Braitbart, L. P., Sirat, G. Y., and Shorte, S. L., "Conical diffraction illumination opens the way for low phototoxicity super-resolution imaging," *Cell Adhesion* **8**, 0–1 (July 2014).

[10] Fallet, C., Caron, J., Oddos, S., Tinevez, J.-Y., Moisan, L., Sirat, G. Y., Braitbart, P. O., and Shorte, S. L., "Conical diffraction as a versatile building block to implement new imaging modalities for superresolution in fluorescence microscopy," in [*Proc. SPIE 9169, Nanoimaging and Nanospectroscopy II*], **9169**(9169) (2014).

[11] Berry, M. V., "Conical diffraction asymptotics: fine structure of Poggendorff rings and axial spike," *Journal of Optics A: Pure and Applied Optics* **6**, 289–300 (Apr. 2004).

[12] Ober, R. J., Ram, S., and Ward, E. S., "Localization Accuracy in Single-Molecule Microscopy," *Biophysical Journal* **86**, 1185–1200 (Feb. 2004).